Dissipationless collapse, weak homology and central cores of elliptical galaxies

Carlo Nipoti[1], Pasquale Londrillo[2] and Luca Ciotti[1]
[1]*Dipartimento di Astronomia, Università di Bologna, via Ranzani 1, 40127 Bologna, Italy*
[2]*INAF - Osservatorio Astronomico di Bologna, via Ranzani 1, 40127 Bologna, Italy*

Accepted 2006 May 10. Received 2006 April 28; in original form 2005 December 13.

ABSTRACT

By means of high-resolution N-body simulations we revisited the dissipationless collapse scenario for galaxy formation. We considered both single-component collapses and collapses of a cold stellar distribution in a live dark matter halo. Single-component collapses lead to stellar systems whose projected profiles are fitted very well by the Sersic $R^{1/m}$ law with $3.6 \lesssim m \lesssim 8$. The stellar end-products of collapses in a dark matter halo are still well described by the $R^{1/m}$ law, but with $1.9 \lesssim m \lesssim 12$, where the lowest m values are obtained when the halo is dominant. In all the explored cases the profiles at small radii deviate from their global best-fit $R^{1/m}$ model, being significantly flatter. The break-radius values are comparable with those measured in 'core' elliptical galaxies, and are directly related to the coldness of the initial conditions. The dissipationless collapse of initially cold stellar distributions in pre-existing dark matter haloes may thus have a role in determining the observed weak homology of elliptical galaxies.

Key words:
galaxies: elliptical and lenticular, cD – galaxies: formation – galaxies: kinematics and dynamics – galaxies: fundamental parameters

1 INTRODUCTION

It is a well established fact that the end-products of dissipationless collapses reproduce several structural and dynamical properties of elliptical galaxies. For example, the pioneering work of van Albada (1982, vA82) showed that the end-products of cold collapses have projected density profiles well described by the $R^{1/4}$ de Vaucouleurs (1948) law, radially decreasing line-of-sight velocity dispersion profiles, and radially increasing velocity anisotropy, in agreement with observations of elliptical galaxies (see also May & van Albada 1984; McGlynn 1984). More recently the dissipationless collapse has been studied in greater detail thanks to the advances in N-body simulations (e.g., see Aguilar & Merritt 1990; Londrillo, Messina & Stiavelli 1991; Udry 1993; Trenti, Bertin & van Albada 2004). These studies show that a smooth final density distribution with $R^{1/4}$ projected mass profile is produced when the initial distribution is cold, extended, and clumpy in phase-space. From the astrophysical point of view the dissipationless collapse (Eggen, Lynden-Bell & Sandage 1962) was introduced to describe a complex physical scenario, in which the gas cooling time of the forming galaxy is shorter than its dynamical (free-fall) time, stars form 'in flight', and the subsequent dynamical evolution is a dissipationless collapse.

From the observational point of view, elliptical galaxies are characterized by a systematic luminosity dependence of their surface brightness profile, the so-called *weak homology*. For example, high quality photometry of elliptical galaxies indicates that the $R^{1/m}$ Sersic (1968) law (see equation 9 below), with best-fit index m ranging from $m \sim 2$ for faint ellipticals up to $m \sim 10$ for the brightest ones, often represents their surface brightness profiles better than the de Vaucouleurs law (the $m = 4$ case; Caon, Capaccioli & D'Onofrio 1993; Prugniel & Simien 1997; Bertin, Ciotti & Del Principe 2002; Graham & Guzmán 2003). In addition, Hubble Space Telescope observations probing the luminosity profiles of several ellipticals down to sub-arcsec resolution (Ferrarese et al. 1994; Lauer et al. 1995) revealed that at these small radii some profiles flatten (core galaxies), others are characterized by steep cusps (power-law galaxies). While the surface brightness profiles of power-law galaxies are well fitted by the $R^{1/m}$ law down to centre, within the break radius R_b the surface brightness profile of core galaxies stay well below their global best-fit Sersic model (Graham et al. 2003; Trujillo et al. 2004; Ferrarese et al. 2006). In general, core profiles are common among bright ellipticals, while faint systems tend to have power-law cusps; remarkably, other galaxy global properties are related to the presence of the core (e.g. Pellegrini 1999, 2005).

The explanation of the observed weak homology of elliptical galaxies is important to understand galaxy formation. For example, the presence of a core is usually inter-

preted as the signature of the merging of supermassive black holes, consequence of the merging of the parent galaxies (e.g. Makino & Ebisuzaki 1996; Faber et al. 1997; Milosavljevic & Merritt 2001), while in N-body simulations of repeated equal-mass dissipationless ('dry') mergers the best-fit m of the end-products increases with their mass (Nipoti, Londrillo & Ciotti 2003a, hereafter NLC03). However, Ciotti & van Albada (2001) and NLC03 showed that repeated dissipationless merging fails to reproduce the Faber & Jackson (1976), the Kormendy (1977), and the $M_{\rm BH}$-σ (Gebhardt et al. 2000, Ferrarese & Merritt 2000) relations, and also that a substantial number of head-on minor mergings make m decrease, bringing the end-products out of the edge-on Fundamental Plane. These results, together with other astrophysical evidences based on stellar population properties such as the $\rm Mg_2$-σ relation (e.g. Burstein et al. 1988; Bender, Burstein & Faber 1993), indicate that dry mergings cannot have had a major role in the formation of elliptical galaxies, and gaseous dissipation is needed (see, e.g., Robertson et al. 2005; Naab et al. 2005).

In alternative (or as a complement) to the merging scenario, it is then of great theoretical interest to explore if (and if yes under what conditions and to what extent) the dissipationless collapse of the stellar population produced by a fast episode of gaseous dissipation and the consequent burst of star formation is able to reproduce end-products with projected density profiles well described by the Sersic law. In particular, given that according to the current cosmological picture galaxies form at peaks of the cold dark matter distribution (e.g. White & Rees 1978; White & Frenk 1991), it is natural to investigate dissipationless collapse in two-component systems. In this work we study this process using high-resolution two-component N-body simulations, in which the collapse of the stellar distribution and the response of the dark matter halo are followed in detail. As will be shown, dissipationless collapses in pre-existing dark matter haloes are indeed able to reproduce surprisingly well the observed weak homology of elliptical galaxies and the flat inner surface brightness profiles of core ellipticals arise naturally from dissipationless collapse, with $R_{\rm b}$ determined by the coldness of the initial conditions.

This paper is organized as follows. The numerical simulations are described in Section 2. The results are presented in Sections 3. Section 4 summarizes.

2 NUMERICAL SIMULATIONS

2.1 Initial conditions

We consider two classes of simulations. In the first we follow the virialization of a cold, single-component density distribution. In the second the initial conditions represent a cold component (stars) deemed to collapse in a nearly-virialized dark matter halo.

The initial conditions consist of the stellar (ρ_*) and the halo ($\rho_{\rm h}$) density distributions, and the corresponding virial ratios β_* and $\beta_{\rm h}$ measure the 'coldness' of the distributions. For example, the stellar virial ratio is defined by

$$\beta_* \equiv \frac{2K_*}{|U_* + W_{*\rm h}|}, \tag{1}$$

where K_* and

$$U_* = -\int < \mathbf{x}\,, \nabla\Phi_* > \rho_* d^3\mathbf{x} \tag{2}$$

are the kinetic energy and the self-gravity of the stellar distribution,

$$W_{*\rm h} = -\int < \mathbf{x}\,, \nabla\Phi_{\rm h} > \rho_* d^3\mathbf{x} \tag{3}$$

is the interaction energy between stars and dark matter, Φ_* and $\Phi_{\rm h}$ are the gravitational potentials of stars and dark matter, respectively, and $<,>$ is the standard inner product. Note that in one-component simulations $\beta_* = 2K_*/|U_*|$. All simulations are evolved up to virialization, which is reached typically within $40t_{\rm dyn}$, where

$$t_{\rm dyn} \equiv \frac{GM_{\rm tot}^{5/2}}{(2|E_{\rm tot}|)^{3/2}} \tag{4}$$

is the dynamical time of the system, and $M_{\rm tot}$ and $E_{\rm tot}$ are its total mass and energy, respectively.

2.1.1 Stellar component

The initial configuration of the stellar component is obtained by introducing inhomogeneity on a smooth, spherically symmetric density distribution ρ_*. In particular, we adopt

$$\rho_*(r) = \frac{3M_* r_*^2}{4\pi(r^2 + r_*^2)^{5/2}} \tag{5}$$

(Plummer 1911), and

$$\rho_*(r) = \frac{3-\gamma}{4\pi}\frac{M_* r_*}{r^\gamma (r_* + r)^{4-\gamma}} \tag{6}$$

with $\gamma = 0$ or $\gamma = 1$ (Dehnen 1993; Tremaine et al. 1994), where M_* is the total mass and r_* the characteristic radius. The particles are spatially distributed according to equations (5) or (6) and then randomly shifted in position (up to $r_*/5$ in modulus), so that the distribution results inhomogeneous.

The velocities of the particles are first randomly extracted from an isotropic Gaussian distribution with a given value of the variance, and we measure the corresponding virial ratio β_0. The required value of the stellar virial ratio $0.002 \lesssim \beta_* \lesssim 0.2$ is then obtained by scaling the velocity of each particle by $\sqrt{\beta_*/\beta_0}$. In some case the stellar distribution is characterized by non-vanishing angular momentum $\mathbf{J}$, which is obtained, for fixed β_*, by modifying the direction of the particles velocity vectors. The system total angular momentum is quantified by the spin parameter

$$\lambda \equiv \frac{|E_{\rm tot}|^{3/2}||\mathbf{J}||}{GM_{\rm tot}^{5/2}}. \tag{7}$$

We consider λ in the range[1] $1.7\times10^{-2} - 1.3\times10^{-1}$ (see Table 1 for details).

[1] We recall that typical values of λ inferred from observations are $\sim 10^{-2}$ for bright ellipticals up to $\sim 10^{-1}$ for faint ellipticals (e.g. Lake 1983).

Table 1. Simulations parameters.

Name	β_*	$\beta_{\rm h}$	$M_{\rm h}/M_*$	$r_*/r_{\rm h}$	N_*	$N_{\rm h}$	ρ_*	$\rho_{\rm h}$	$\lambda/10^{-2}$	c/a	b/a	m_a	m_b	m_c	ϵ_a	ϵ_b	ϵ_c
pl04n0002	0.002	-	0	-	409600	-	P	-	0	0.47	0.97	4.3 ± 0.06	4.2 ± 0.08	3.6 ± 0.1	0.52	0.54	0.05
pl04n0005	0.005	-	0	-	409600	-	P	-	0	0.46	0.93	4.3 ± 0.07	4.2 ± 0.1	3.8 ± 0.1	0.50	0.53	0.09
pl1o001	0.01	-	0	-	102400	-	P	-	1.74	0.44	0.81	4.6 ± 0.08	3.7 ± 0.2	3.6 ± 0.2	0.43	0.59	0.26
pl5o001	0.01	-	0	-	102400	-	P	-	3.63	0.55	0.75	5.2 ± 0.2	4.4 ± 0.09	3.7 ± 0.2	0.29	0.49	0.26
pl10o001	0.01	-	0	-	102400	-	P	-	3.70	0.56	0.75	5.0 ± 0.2	4.9 ± 0.1	3.9 ± 0.1	0.27	0.49	0.28
pl20o001	0.01	-	0	-	102400	-	P	-	3.75	0.57	0.80	4.5 ± 0.2	4.4 ± 0.1	3.9 ± 0.1	0.28	0.47	0.23
pl20f001	0.01	-	0	-	102400	-	P	-	4.98	0.24	0.32	5.1 ± 0.2	4.6 ± 0.09	3.9 ± 0.09	0.38	0.53	0.23
pl04n001	0.01	-	0	-	409600	-	P	-	0	0.47	0.97	4.2 ± 0.07	4.1 ± 0.09	3.7 ± 0.1	0.50	0.53	0.05
hq2r001	0.01	-	0	-	204800	-	1	-	0	0.47	0.78	5.7 ± 0.3	5.1 ± 0.2	4.7 ± 0.2	0.37	0.51	0.23
pl20f002	0.02	-	0	-	102400	-	P	-	7.09	0.49	0.68	4.6 ± 0.1	4.6 ± 0.1	4.0 ± 0.06	0.38	0.53	0.23
pl2r002	0.02	-	0	-	204800	-	P	-	0	0.48	0.87	4.0 ± 0.1	3.8 ± 0.1	3.6 ± 0.1	0.42	0.51	0.13
hq2r002	0.02	-	0	-	204800	-	1	-	0	0.48	0.88	6.0 ± 0.2	5.7 ± 0.3	5.4 ± 0.3	0.41	0.49	0.12
g02r002	0.02	-	0	-	204800	-	0	-	0	0.49	0.93	6.2 ± 0.2	6.3 ± 0.2	5.3 ± 0.2	0.49	0.52	0.10
pl04n0025	0.025	-	0	-	409600	-	P	-	0	0.46	0.63	4.5 ± 0.3	3.8 ± 0.1	3.8 ± 0.2	0.22	0.50	0.40
pl20c005	0.05	-	0	-	102400	-	P	-	12.6	0.49	0.62	4.7 ± 0.1	3.8 ± 0.1	4.0 ± 0.05	0.20	0.53	0.41
pl1n005	0.05	-	0	-	1024000	-	P	-	0	0.40	0.66	4.4 ± 0.2	4.0 ± 0.1	3.7 ± 0.2	0.35	0.58	0.37
pl04n005	0.05	-	0	-	409600	-	P	-	0	0.41	0.70	4.3 ± 0.2	4.0 ± 0.2	3.6 ± 0.2	0.38	0.57	0.33
hq2r005	0.05	-	0	-	204800	-	1	-	0	0.41	0.44	8.1 ± 0.5	6.2 ± 0.2	6.2 ± 0.2	0.11	0.62	0.58
pl04n01	0.1	-	0	-	409600	-	P	-	0	0.96	0.97	4.0 ± 0.3	4.2 ± 0.3	3.8 ± 0.3	0.01	0.04	0.03
hq2r01	0.1	-	0	-	204800	-	1	-	0	0.39	0.40	7.4 ± 0.6	5.3 ± 0.2	5.2 ± 0.2	0.02	0.63	0.64
g02r01	0.1	-	0	-	204800	-	0	-	0	0.42	0.46	7.5 ± 0.5	5.0 ± 0.1	5.2 ± 0.2	0.08	0.59	0.56
pl04n02	0.2	-	0	-	409600	-	P	-	0	0.96	0.97	3.6 ± 0.3	3.7 ± 0.3	4.0 ± 0.4	0.01	0.01	0.01
hq2r02	0.2	-	0	-	204800	-	1	-	0	0.98	0.99	5.6 ± 0.3	5.6 ± 0.3	5.6 ± 0.3	0.01	0.02	0.01
hpl4r05m001	0.01	0.7	0.5	4	163840	81920	P	1	0	0.28	0.40	4.3 ± 0.2	3.1 ± 0.1	3.1 ± 0.1	0.35	0.75	0.63
hpl4r1m001	0.01	0.8	1	4	102400	102400	P	1	0	0.24	0.34	3.7 ± 0.1	2.8 ± 0.07	2.8 ± 0.06	0.31	0.77	0.68
hpl20f4r1m001	0.01	0.8	1	4	102400	102400	P	1	3.14	0.24	0.32	3.8 ± 0.1	2.7 ± 0.07	2.7 ± 0.06	0.28	0.79	0.71
g0pl04r1m001	0.01	0.3	1	0.4	102400	102400	P	0	0	0.37	0.57	3.3 ± 0.05	2.9 ± 0.06	2.9 ± 0.05	0.35	0.64	0.46
g0pl08r1m001	0.01	0.3	1	0.8	102400	102400	P	0	0	0.43	0.87	4.3 ± 0.09	3.7 ± 0.08	3.6 ± 0.1	0.48	0.56	0.13
hpl025r2m002	0.02	0.4	2	0.25	102400	204800	P	1	0	0.34	0.35	3.4 ± 0.1	3.1 ± 0.03	3.0 ± 0.03	0.0	0.68	0.68
plpl05r2m002	0.02	0.1	2	0.5	204800	409600	P	P	0	0.30	0.34	4.0 ± 0.1	3.4 ± 0.04	3.9 ± 0.1	0.22	0.71	0.71
plpl05r5m002	0.02	0.02	5	0.5	81920	409600	P	P	0	0.47	0.72	4.8 ± 0.1	4.0 ± 0.1	4.8 ± 0.1	0.32	0.49	0.29
g0hq05r2m002	0.02	1	2	0.5	204800	204800	1	0	0	0.42	0.85	5.4 ± 0.2	5.6 ± 0.3	5.2 ± 0.2	0.49	0.57	0.17
hus20r1m002	0.02	0.9	1	20	102400	102400	U	1	0	0.87	0.90	5.6 ± 0.4	6.5 ± 0.6	5.6 ± 0.4	0.01	0.11	0.11
hpl4r1m005	0.05	0.8	1	4	102400	102400	P	1	0	0.98	0.99	2.5 ± 0.03	2.5 ± 0.04	2.5 ± 0.04	0.01	0.01	0.01
hpl4r2m005	0.05	0.8	2	4	102400	204800	P	1	0	0.99	1.00	2.2 ± 0.03	2.3 ± 0.04	2.2 ± 0.03	0.01	0.00	0.00
hpl8r2m005	0.05	0.9	2	8	102400	204800	P	1	0	0.99	1.00	2.0 ± 0.03	1.9 ± 0.02	1.9 ± 0.02	0.00	0.01	0.01
hpl2r4m005	0.05	0.8	4	2	81920	327680	P	1	0	0.99	1.00	2.1 ± 0.03	2.1 ± 0.03	2.1 ± 0.03	0.00	0.01	0.00
npl4r2m005	0.05	0.9	2	4	102400	204800	P	N	0	0.33	0.33	3.4 ± 0.2	2.8 ± 0.09	2.8 ± 0.08	0.01	0.01	0.01
npl4r4m005	0.05	1	4	4	81920	327680	P	N	0	0.97	0.98	2.4 ± 0.05	2.3 ± 0.04	2.3 ± 0.05	0.01	0.00	0.00
g15pl4r2m005	0.05	1	2	4	102400	204800	P	1.5	0	0.98	0.99	1.9 ± 0.04	2.0 ± 0.05	2.0 ± 0.04	0.01	0.02	0.00
g0pl4r1m005	0.05	0.7	1	4	102400	102400	P	0	0	0.33	0.33	3.2 ± 0.2	2.8 ± 0.06	2.7 ± 0.07	0.01	0.70	0.70
g0hq05r1m005	0.05	0.2	1	0.5	102400	102400	1	0	0	0.39	0.39	12.1 ± 1.2	7.3 ± 0.3	7.8 ± 0.4	0.03	0.64	0.63
hpl2r2m01	0.1	0.8	2	2	102400	204800	P	1	0	0.98	0.99	2.6 ± 0.1	2.6 ± 0.1	2.6 ± 0.1	0.01	0.03	0.02

First column: name of the simulation. β_* and $\beta_{\rm h}$: initial stellar and halo virial ratios, respectively. $M_{\rm h}/M_*$: halo to stellar mass ratio. $r_*/r_{\rm h}$; ratio of initial characteristic radii. N_* and $N_{\rm h}$: number of stellar and halo particles. ρ_* and $\rho_{\rm h}$: initial stellar and halo distribution (P, N, U: Plummer, NFW, and uniform spheres distributions, respectively. Numbers identify $\gamma = 0$, 1, 1.5 models.). λ: spin parameter. c/a and b/a: minor-to-major and intermediate-to-major axis ratios. m_a, m_b, m_c and ϵ_a, ϵ_b, ϵ_c: best-fit Sersic indices and ellipticities for projections along the principal axes.

2.1.2 Halo component

In most of the simulations the dark matter halo component is represented by a γ-model distribution

$$\rho_{\rm h}(r) = \frac{3-\gamma}{4\pi}\frac{M_{\rm h} r_{\rm h}}{r^{\gamma}(r_{\rm h}+r)^{4-\gamma}}, \qquad (8)$$

where $M_{\rm h}$ is the total mass, $r_{\rm h}$ is the characteristic radius, and we adopt $\gamma = 0$, 1, or 1.5. In two simulations the halo component is represented by a Navarro, Frenk & White (1996, NFW) density profile with scale radius $r_{\rm h}$, truncation radius $10r_{\rm h}$, and total mass $M_{\rm h}$. Note that for the $\gamma = 1$ model (Hernquist 1990) $\rho_{\rm h}(r) \sim r^{-1}$ for $r \to 0$, as in the NFW density profile. The velocity distribution of the halo particles is isotropic and, with few exceptions, such that the halo would be in equilibrium in the absence of the stellar component. In practice, in most cases the halo is nearly-virialized ($0.7 \lesssim \beta_{\rm h} \lesssim 1$), while in a subset of simulations the halo is strongly out of equilibrium ($\beta_{\rm h} \ll 1$; see Table 1 and Section 3.4). Length-scale ratios $r_*/r_{\rm h}$, and mass ratios $M_{\rm h}/M_*$ characterizing the initial conditions are listed in Table 1.

2.2 Numerical methods

Numerically, the initial distribution of particles in phase-space is realized as described in Nipoti, Londrillo & Ciotti (2002). For the stellar distribution we use typically $N_* \sim 1-4\times10^5$ particles, and in the two-component cases the number of particles $N_{\rm h}$ of the dark matter distribution is such that halo and stellar particles have the same mass (with few exceptions in which halo particles are twice as massive as stellar particles; see Table 1).

For the simulations we used the parallel N-body code FVFPS (Fortran Version of a Fast Poisson Solver; Londrillo, Nipoti & Ciotti 2003; NLC03), based on Dehnen's (2000, 2002) scheme. We adopt the following values for the code parameters: minimum value of the opening parameter $\theta_{\rm min} = 0.5$, and softening parameter $\varepsilon = 0.005 - 0.025$ in units of r_* (depending on the number of particles). The time-step Δt, which is the same for all particles, is allowed to vary adaptively in time as a function of the maximum particle density $\rho_{\rm max}$. In particular, we adopted $\Delta t = 0.3/\sqrt{(4\pi G\rho_{\rm max})}$, the classical time-step criterion for the stability of the leap-frog time integration. This gives time-steps as small as $6\times10^{-4}t_{\rm dyn}$ during the first phases of the coldest collapses, assuring energy conservation to within $10^{-3}-10^{-4}$. In order to estimate discreteness effects, we ran several test simulations varying the softening length ε and the number of particles. We found that the main properties of the end-product of a simulation with $N_* \sim 10^6$ are not significantly different from those of lower-resolution simulations with the same initial conditions. In particular, the tests indicate that, for a one-component simulation with $N_* \sim 4\times10^5$ and $\varepsilon = 0.01r_*$, the final density distribution can be trusted down to radii $\sim 2\varepsilon$ ($\sim 0.01\,r_{\rm M}$, where $r_{\rm M}$ is the half-mass radius), in accordance with numerical convergence studies (e.g. Power et al. 2003).

The intrinsic and projected properties of the end-products are determined following Nipoti et al. (2002), while the position of the centre of the system is determined using the iterative technique described by Power et al. (2003). In particular, we measure the axis ratios c/a and b/a of the inertia ellipsoid (where a, b and c are the major, intermediate and minor axis) of the stellar component, their angle-averaged density distribution and half-mass radius $r_{\rm M}$. For each end-product, in order to estimate the importance of projection effects, we consider three orthogonal projections along the principal axes of the inertia tensor, measuring the ellipticity $\epsilon = 1 - b_{\rm e}/a_{\rm e}$, the circularized projected density profile and the circularized effective radius $R_{\rm e} \equiv \sqrt{a_{\rm e}b_{\rm e}}$ (where $a_{\rm e}$ and $b_{\rm e}$ are the major and minor semi-axis of the effective isodensity ellipse). We fit (over the radial range $0.1 \lesssim R/R_{\rm e} \lesssim 10$) the circularized projected stellar density profile of the end-products with the $R^{1/m}$ Sersic (1968) law:

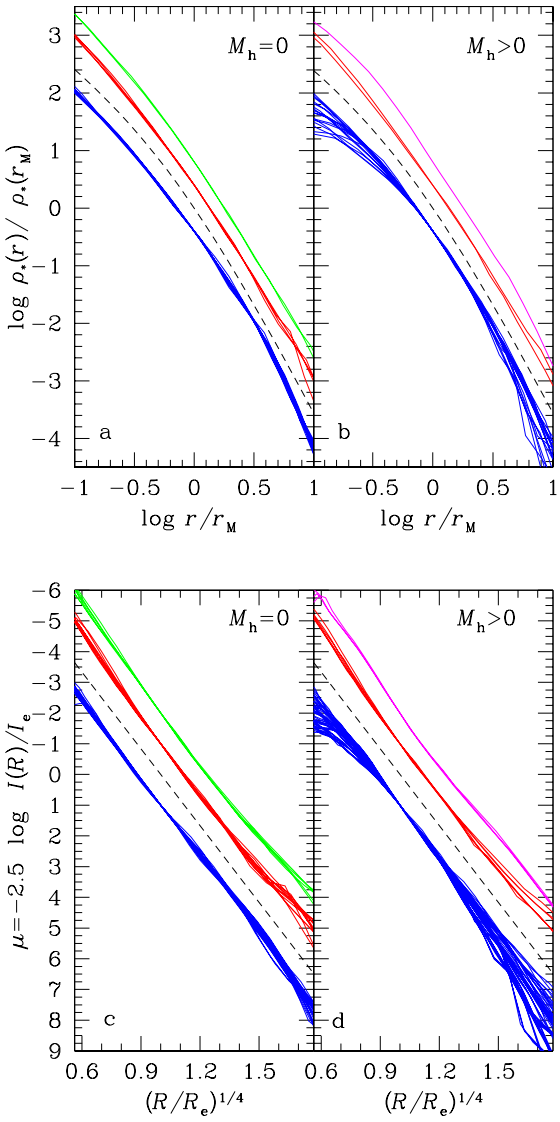

Figure 1. Angle-averaged spatial density profile of the end-products of one-component collapses (panel a; solid lines) and of the stellar component of two-component collapses (panel b; solid lines). The dashed line is the $\gamma = 1.5$ profile. Panels c and d: projected density profiles (along the principal axes) of the stellar component of the end-products of one- and two-component collapses. The dashed line represents the $R^{1/4}$ law. Different colours indicate different initial stellar density profiles: Plummer (blue), $\gamma = 1$ model (red), $\gamma = 0$ model (green), hus20r1m002 (magenta, see Table 1). Blue, red, green and magenta curves are vertically offset by -0.3, 0.3, 0.6 and 0.6 dex (top panels), and by 1, -1, -2, and -2 magnitudes (bottom panels), respectively.

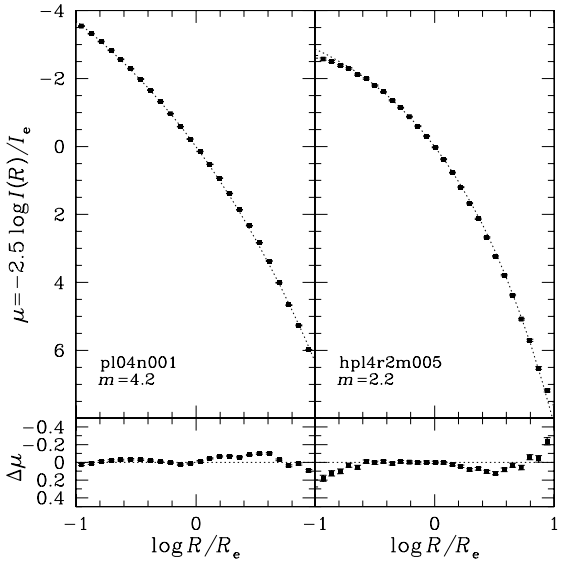

Figure 2. Circularized projected stellar density profiles of the end-products of representative one-component (left) and two-component (right) collapses. The dotted lines are the best-fitting Sersic models. 1-σ error bars are also plotted.

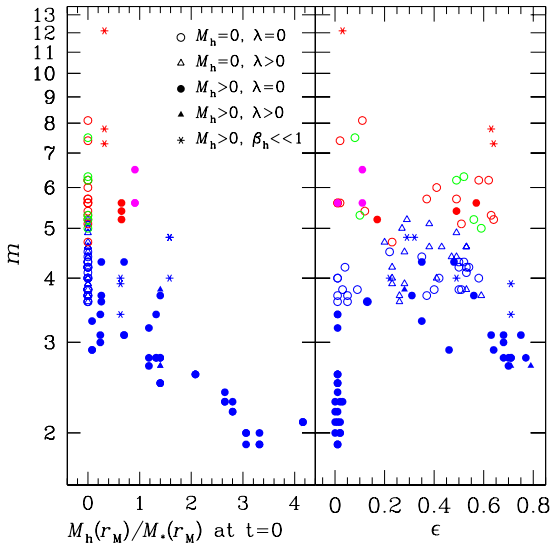

Figure 3. Left: best-fit Sersic parameter m as function of the initial dark-to-luminous mass ratio $M_{\rm h}(r_{\rm M})/M_*(r_{\rm M})$ within the half-mass radius of the stellar distribution. Right: best-fit Sersic index as a function of the ellipticity. For each model we plot three points corresponding to the three principal projections. Colours have the same meaning as in Fig. 1.

$$I(R) = I_{\rm e}\,\exp\left\{-b(m)\left[\left(\frac{R}{R_{\rm e}}\right)^{1/m}-1\right]\right\}, \qquad (9)$$

where $I_{\rm e}\equiv I(R_{\rm e})$ and $b(m)\simeq 2m-1/3+4/(405m)$ (Ciotti & Bertin 1999). In the fitting procedure m is the only free parameter, because $R_{\rm e}$ and $I_{\rm e}$ are determined by their *measured* values obtained by particle count.

3 PROPERTIES OF THE END-PRODUCTS

3.1 Density distribution

3.1.1 Spatial density profile

In Fig. 1a we plot the angle-averaged density profiles of the end-products of one-component collapses (solid lines). The relatively small spread of the curves in the diagram indicates that the profiles are similar over most of the radial range ($0.1\lesssim r/r_{\rm M}\lesssim 10$), independently of the details of the initial density distribution and of the specific angular momentum. In particular the profiles are reasonably well described by the $\gamma=1.5$ model (dashed line).

In Fig. 1b we plot the angle-averaged density profiles of the stellar component of two-component simulations. The final stellar density profiles of two-component collapses are more varied than the results of one-component collapses, and they are typically flatter at $r<r_{\rm M}$ and steeper at $r>r_{\rm M}$ than the $\gamma=1.5$ model. So the overall (and expected) effect of the presence of the halo in the collapse is to introduce significant structural homology.

The initial and final halo density distributions are very similar when the halo is dominant ($M_{\rm h}/M_*\geq 2$). When $M_{\rm h}/M_*\leq 1$ the halo profile in the central regions is significantly modified by the collapse. In particular, the final inner halo profile is shallower than the initial one if $r_*/r_{\rm h}\gtrsim 1$ at $t=0$, and steeper if $r_*/r_{\rm h}\lesssim 1$. Thus, the collapsing stellar component may be able to modify the density distribution of a pre-existing halo[2]. The final total (stellar plus halo) density profiles are characterized by significant structural non-homology, and are typically well represented by γ-models with $0\lesssim\gamma\lesssim 2$.

Finally, we note that in both one- and two-component simulations the final density distribution tends to be steeper when the initial stellar distribution is a $\gamma=0$ (green curves in Fig. 1) or a $\gamma=1$ (red curves) model than for Plummer initial conditions (blue curves; see also Section 3.4).

3.1.2 Projected density profile: Sersic fit

The projected density profiles of the stellar end-products are analysed as described in Section 2.2. The fitting radial range $0.1\lesssim R/R_{\rm e}\lesssim 10$ is comparable with or larger than the typical ranges spanned by observations (e.g. Bertin et al. 2002). The best-fit Sersic indices m_a, m_b and m_c (for projections along the axes a, b, and c, respectively) are reported in Table 1, together with the 1σ uncertainties corresponding to $\Delta\chi^2=1$. We note that the relative uncertainties on the best-fit Sersic indices are in all cases smaller than 10 per cent.

Figure 1c shows the circularized projected density profiles of the end-products of one-component simulations (three projections for each system, each normalized to the corresponding value of $I_{\rm e}$), while the de Vaucouleurs profile is the dashed straight line. Apparently all the end-products of one-component collapses do not deviate strongly from the $R^{1/4}$ law over most of the radial range, in agreement with previous studies (vA82, Londrillo et al. 1991, Trenti et al. 2004). In particular, the Sersic index is found in the range

[2] Analytical restrictions on the relative density radial trend of stars and dark matter have been derived in Ciotti & Pellegrini (1992), and Ciotti (1996; 1999).

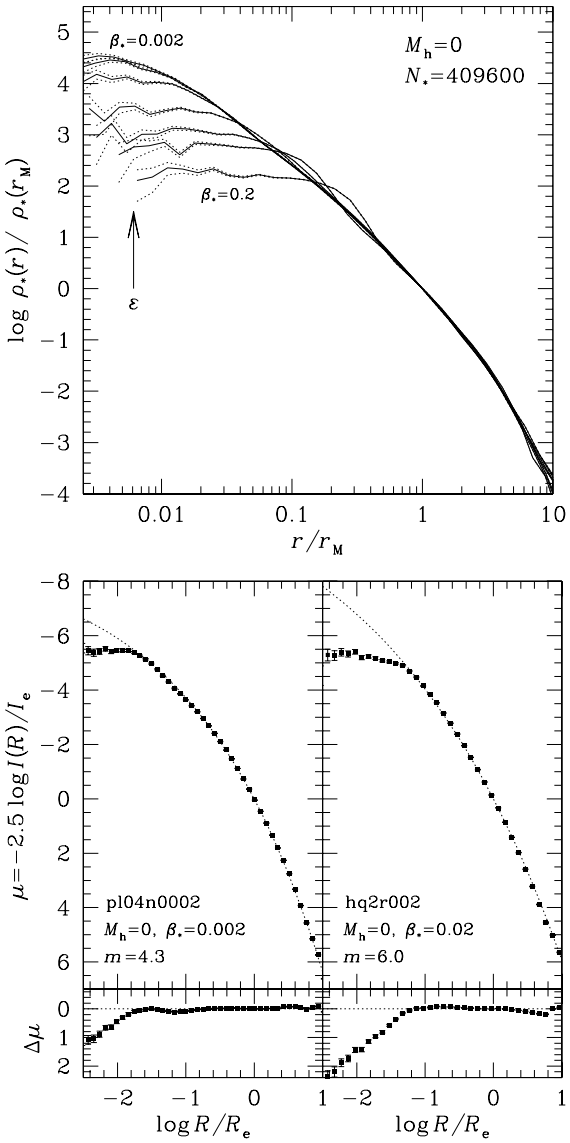

Figure 4. Top: angle-averaged density profiles of the end-products of one-component simulations with $\beta_* = 0.002$, 0.005, 0.01, 0.025, 0.05, 0.1 and 0.2 (solid lines). The arrow indicates the typical simulation softening-length ε, while dotted curves indicate 1-σ uncertainties due to statistical noise. Bottom: circularized projected density profiles of two representative one-component collapses. The bars are 1-σ uncertainties. The dotted lines are the best-fitting Sersic models over the radial range $0.1 < R/R_e < 10$.

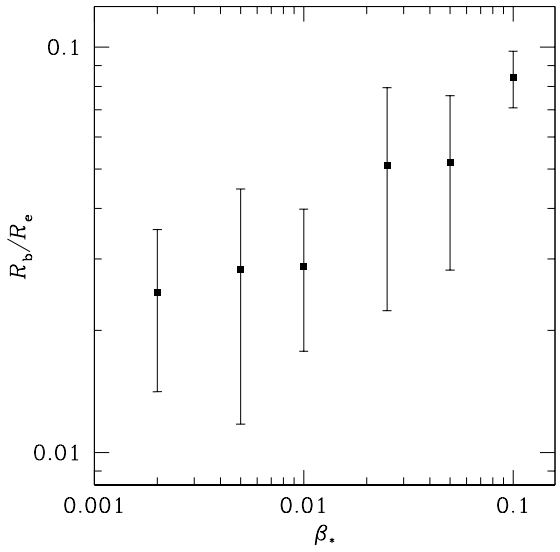

Figure 5. Break radius normalized to the effective radius as a function of the initial virial ratio for the simulations in Fig. 4 (top) with $\beta_* \leq 0.1$. The symbols refer to the average among the three considered projections values, which span the range represented by the vertical bars.

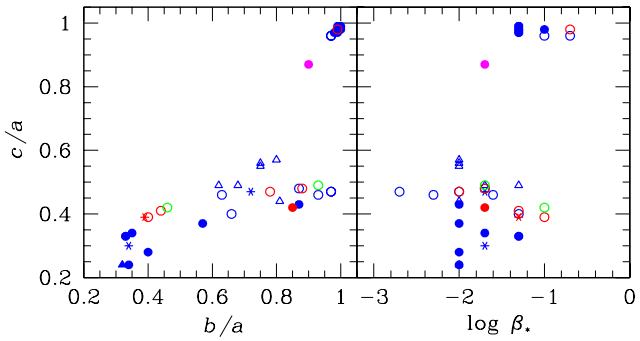

Figure 6. Final axis ratios c/a as a function of b/a (left), and of the initial stellar virial ratio β_* (right). The meaning of symbols and colours is the same as in Fig. 3.

$3.6 \lesssim m \lesssim 8$. The quality of the fits is apparent in Fig. 2 (left), which plots the surface brightness profile of a projection of one of these end-products, together with the best-fit ($m = 4.2 \pm 0.07$) Sersic law, and the corresponding residuals. The average residuals between the data and the fits are typically $0.04 \lesssim \langle \Delta\mu \rangle \lesssim 0.2$, where $\mu = -2.5 \log I(R)/I_e$.

In Fig. 1d we finally plot the circularized projected stellar density profiles of the end-products of two-component simulations. These systems deviate systematically from the $R^{1/4}$ (straight line), and in most cases the profile remain below it at small and large radii. For these systems we found $1.9 \lesssim m \lesssim 12$, with average residuals in the same range as those of one-component collapses. We note that values of m significantly larger than 4 are found only for collapses starting from sufficiently concentrated stellar distributions (see Section 3.4). Figure 2 (right) plots the projected profile of a representative two-component simulation with $M_h/M_* = 2$ together with the best-fit ($m = 2.2 \pm 0.03$) model and the residuals.

The situation is summarized in the left panel of Fig. 3, where it is apparent how the initial amount and concentration of the dark matter is crucial in determining the final shape of the profile. In particular, the trend is that m is anti-correlated with the initial ratio $M_h(r_M)/M_*(r_M)$ within r_M. However, it is also apparent from Fig. 3 that there is significant spread in m for similar values of $M_h(r_M)/M_*(r_M)$, which reflects differences in the initial stellar density profiles and halo virial ratios (see Section 3.4). We also note that for some strongly aspherical end-products m_a, m_b, and m_c are significantly different (see Table 1).

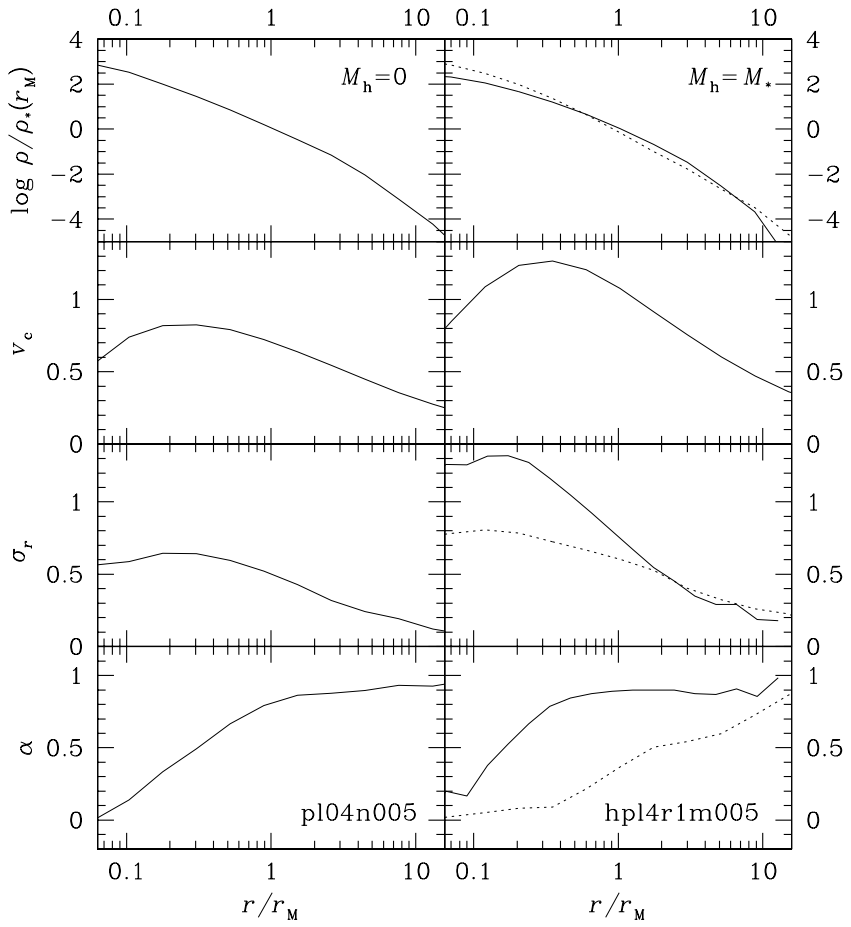

Figure 7. Density, circular velocity, radial velocity dispersion, and anisotropy parameter for the end-products of a one-component simulation (left panels) and a two-component simulation (right panels). Solid lines refer to stars; dashed lines to dark matter. Velocities are normalized to $\sqrt{GM_*/r_M}$.

3.1.3 Behaviour at small radii

So far we have considered the properties of intrinsic and projected density profiles at radii $\gtrsim 0.1r_M$ (and $0.1R_e$). We now focus on the behaviour of the profiles at smaller radii, yet confining our discussion to $r \gtrsim 0.01\, r_M$ where artificial numerical effects do not affect the profile (see Section 2.2).

As apparent from Fig. 4 (top), the end-product density profiles of one-component collapses have flat cores at $r \lesssim 0.1r_M$, in agreement with previous studies (vA82; May & van Albada 1984). Correspondingly, the projected density profiles are characterized by a break radius R_b, in the sense that for $R < R_b$ they stay below the best-fit Sersic profiles over $0.1 < R/R_e < 10$, as shown in Fig. 4 (bottom panels), for a case with $\beta_* = 0.002$ (left) and a case with $\beta_* = 0.02$ (right). Thus, β_* determines the radial range over which the final surface density profile is well fitted by the Sersic law, with colder initial conditions producing smaller cores (see Fig. 5). Note that we do not represent R_b/R_e for $\beta_* = 0.2$, because in this case the core extends to $R \gtrsim 0.1R_e$, affecting the Sersic fit in the considered radial range $0.1 < R/R_e < 10$, so the break radius is not well defined.

Also the projected density profiles of two-component end-products flatten at small radii and deviate from an inwards extrapolation of the best-fitting Sersic law. However, the flattening is typically more gradual and the break is not as apparent as in the one-component cases. This is in part due to the fact that the stellar end-products of two-component simulations are characterized in general by smaller m, corresponding to quite shallow profiles.

3.1.4 Intrinsic shape and projected ellipticity

Figure 6 shows the location of the end-products in the (b/a, c/a) and (β_*, c/a) planes. The final states of one-component collapses are roughly spherical for $\beta_* \gtrsim 0.1$, prolate ($c/a \sim b/a \sim 0.3$) for $0.05 \lesssim \beta_* \lesssim 0.1$ and oblate ($c/a \sim c/b \sim 0.5$) for $\beta_* \lesssim 0.05$, in agreement with the findings of previous works (Aguilar & Merritt 1990; Londrillo et al. 1991). A similar behaviour is found in two-component simulations, though in this case the halo mass and concentration, beside β_*, play a role in determining the final shape of the stellar component. In particular, in case of dominant halo the remnant is roughly spherical even for $\beta_* = 0.02 - 0.05$. When the stellar component develops a bar, the dark matter halo becomes mildly flattened ($c/a \sim b/a \sim 0.7 - 0.8$).

The ellipticity ϵ (measured for each of the principal projections of each end-product) is found in the range $0 - 0.8$, consistent with those observed in real ellipticals, and no significant correlation with the Sersic index m is found (Fig. 3, right panel). In particular, $m \gtrsim 4$ systems span a wide range

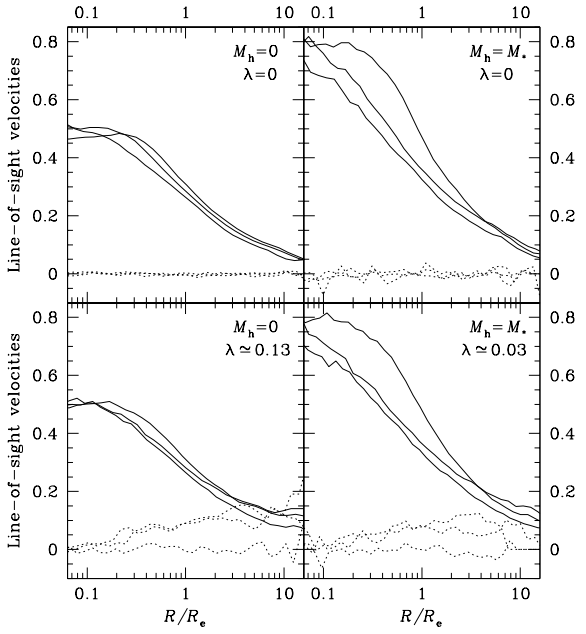

Figure 8. Line-of-sight velocity (dotted line) and velocity dispersion (solid line), along the principal axes, normalized to $\sqrt{GM_*/R_e}$, for the stellar component of four end-products with different values of M_h and λ.

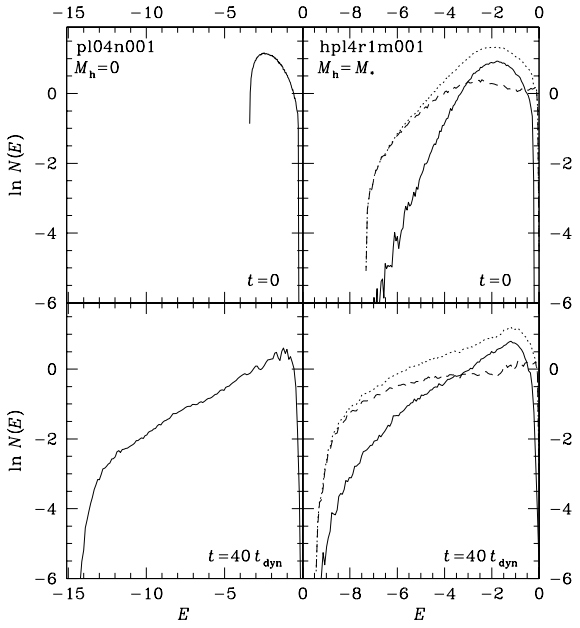

Figure 9. Left panels: initial (top) and final (bottom) differential energy distribution for a representative one-component simulation. Right panels: same as left panels for a two-component simulation. Solid, dashed and dotted curves refer to the stellar, halo, and total distributions, respectively. The energy per unit mass E is normalized to $E_{\rm tot}/M_{\rm tot}$.

in ellipticity, while lower-m systems are found both round and very flattened (though m as low as 2 is found only for $\epsilon\sim0$).

3.2 Kinematics

The internal dynamics of the end-products is quantified by a 'bona fide' circular velocity $v_c^2\equiv GM_{\rm tot}(r)/r$, the (angle-averaged) radial component σ_r of the velocity dispersion tensor, and the anisotropy parameter $\alpha(r)\equiv1-0.5\sigma_{\rm t}^2/\sigma_r^2$, where $\sigma_{\rm t}$ is the tangential component of the velocity-dispersion tensor. These quantities, together with the corresponding angle-averaged density distributions, are shown in Fig. 7 for two representative simulations. The radial dependence of v_c, σ_r and α is qualitatively similar in the one- and two-component cases. The circular velocity is roughly constant for $0.2\lesssim r/r_{\rm M}\lesssim1$ and decreases inwards and outwards; σ_r has a plateau at small radii and decreases at larger radii. The systems are approximately isotropic in the centre ($\alpha\sim0$) and strongly radially anisotropic for $r\gtrsim r_{\rm M}$, in agreement with previous results (e.g. vA82; Trenti et al. 2004).

For each model projection we compute the line-of-sight streaming velocity $v_{\rm los}$ and the line-of-sight velocity dispersion $\sigma_{\rm los}$, considering particles in a slit of width $R_e/4$ around the semi-major axis of the isophotal ellipse. Figure 8 plots $v_{\rm los}$ (solid line) and $\sigma_{\rm los}$ (dashed line) of the stellar component for four systems with different combinations of dark matter mass M_h and spin parameter λ. The projected velocity dispersion profiles do not present the central depressions characterizing the isotropic Sersic profiles or the Hernquist model. In the presence of significant angular momentum (bottom panels) $v_{\rm los}$ becomes comparable with $\sigma_{\rm los}$ at $R\sim$ few R_e when the line-of-sight direction and the angular momentum vector are orthogonal.

3.3 Differential energy distribution

In Fig. 9 (left panels) we plot the initial (top) and final (bottom) differential energy distributions $N(E)$ (i.e. the number of particles with energy per unit mass between E and $E+dE$) for a representative one-component collapse simulation. The final differential energy distribution is well represented by an exponential $N(E)\propto\exp(\eta E)$, over most of the energy range, with $\eta\sim2.1$ (when the energy per unit mass is normalized to GM_*/R_e, see Binney 1982; van Albada 1982; Ciotti 1991). We find that the colder the initial conditions, the larger the range in E in which $N(E)$ is exponential, because only very cold initial conditions produce strongly bound particles (and, correspondingly, populate the very central regions; see Section 3.1.3).

In the right panels we plot, for a representative two-component collapse, the initial and final $N(E)$ of the stellar (solid lines) and halo (dashed lines) component, together with the total $N(E)$ (dotted lines). Note how the energy distribution of the final stellar component is steeper than the halo component, i.e., how the very-bound end of the energy distribution (typically corresponding to particles in the central region of the density distribution) is populated by halo particles (dashed line), while most of the stellar particles are close to $E\sim0$. Interestingly, the slope of the total differential energy distribution (dotted line) is very similar to that found in the one-component case when E is normalized to $E_{\rm tot}/M_{\rm tot}$.

3.4 Exploring different initial conditions

In general, the large-scale properties of the end-products of one-component simulations do not depend strongly on the initial distribution, provided that it is clumpy and cold

enough. However, some information on the initial distribution is not completely erased during the collapse. As apparent from Fig. 3, while Plummer (blue symbols) initial conditions lead to systems very close to the de Vaucouleurs law ($3.6 \lesssim m \lesssim 5.2$), the end-products of $\gamma = 0$ (green symbols) and $\gamma = 1$ (red symbols) initial distributions are characterized by higher Sersic indices ($5 \lesssim m \lesssim 8$).

In two-component simulations the initial shape of the dark matter halo does not have strong influence on the properties of the stellar end-product. In particular, for a wide range of halo density profiles ($\gamma = 0$, $\gamma = 1$, $\gamma = 1.5$, and NFW distributions), the final stellar density profiles have $m \lesssim 4$, down to 2, if the halo is sufficiently concentrated. If the halo is light and/or extended, independently of its shape, the final stellar components have $m \gtrsim 4$. We also considered cases in which the halo, as well as the stellar component, is strongly out of equilibrium ($\beta_{\rm h} \ll 1$; see Table 1). Independently of the details of their initial halo density distributions, the stellar end-products of these simulations have global properties more similar to one-component collapses than to collapses in nearly virialized haloes. As a consequence, these end-products (represented as stars in Fig. 3), contribute significantly to the scatter in the left diagram of Fig. 3, because they typically have higher values of m than the collapses in nearly virialized haloes with similar dark-to-luminous mass ratio. In addition, in analogy with the one-component case, two-component collapses with $\gamma = 1$ initial stellar distribution (such as g0hq05r2m002, red filled circles in Fig. 3) produce systems with higher Sersic index than those with Plummer initial distribution (blue symbols) with similar dark-to-luminous mass ratio (see Fig. 3, left panel). Interestingly, the stellar system with the highest Sersic index ($m \simeq 12.1$) was obtained starting with a $\gamma = 1$ stellar distribution embedded in a collapsing dark matter halo (simulation g0hq05r1m005, red stars in Fig. 3).

We also considered a rather extreme case of two-component initial conditions (model hus20r1m002 in Table 1, magenta curves and symbols in Fig. 1, 3, and 6) that could be also interpreted as a multiple merging experiment. The halo is a Hernquist model with core radius $r_{\rm h}$, and the stars are distributed in 20 uniform spheres of radius $2r_{\rm h}$, whose centres of mass are uniformly distributed in a sphere of radius $20r_{\rm h}$. Each small sphere is cold, having all particles at rest with respect to its centre of mass. So the small spheres collapse first because of self-gravity and then merge because of dynamical friction, finally forming a stellar system with best-fit Sersic index[3] $m \sim 6.5$. We note that in this case the final central halo density distribution is significantly flatter than the the initial one, as expected as a consequence of dynamical friction heating (see also Nipoti et al. 2004).

According to these results, it appears that the only way to produce $m \gtrsim 5$ systems with dissipationless processes is either merging or collapse starting from concentrated and cold initial distributions, while dissipationless collapses of more diffuse, cold distributions lead to $m \lesssim 5$ systems. We note that lower values of m were also found as a result of quite different dissipationless processes: Merritt et al. (2005) found that the projected density of the dark matter haloes of cosmological N-body simulations are well fitted by the Sersic law with $2 \lesssim m \lesssim 4$, while Nipoti et al. (2002) obtained $1 \lesssim m \lesssim 5$ for the end-products of radial orbit instability.

[3] Similar values of m were also found by Nipoti et al. (2003b) for the end-products of galactic cannibalism simulations.

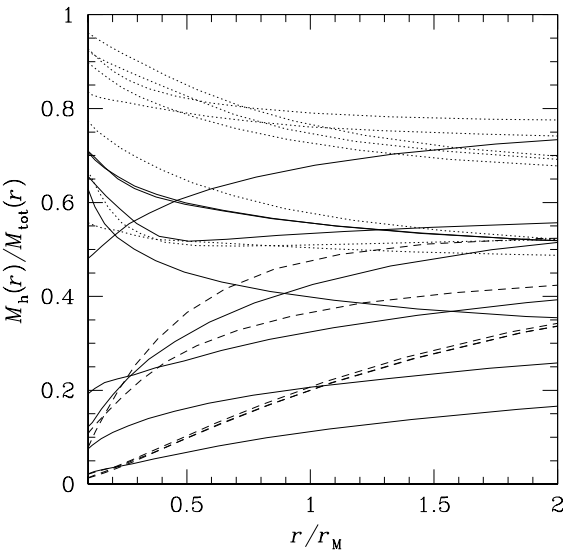

Figure 10. Dark-to-total mass inside r for the end-products of the two-component simulations. Dotted, solid, and dashed curves refer to systems with average best-fitting Sersic index $\langle m \rangle \leq 3$, $3 < \langle m \rangle < 5$, and $\langle m \rangle \geq 5$, respectively [$\langle m \rangle = (m_a + m_b + m_c)/3$].

4 DISCUSSION AND CONCLUSIONS

Before summarizing the main results of the numerical simulations, it is useful to list three (of the several) *observational* properties of ellipticals that should be explained by any plausible formation (or evolutionary) scenario:

(i) The best-fit Sersic index increases from $m \sim 2$ to $m \sim 10$ from faint to luminous galaxies (Caon et al. 1993; Bertin et al. 2002). Thus, the light profiles of luminous ellipticals as a function of $R/R_{\rm e}$ are *steeper* for $R \lesssim R_{\rm e}$ and flatter for $R \gtrsim R_{\rm e}$ than the profiles of low-luminosity ellipticals (see, e.g., Ciotti 1991).

(ii) However, the light profiles of luminous ellipticals present a flat core in their very central regions, deviating from the global best-fit Sersic law. The profiles of low-luminosity ellipticals are instead well fitted by the Sersic law down to the centre (e.g. Lauer et al. 1995; Trujillo et al. 2004), so in the very central regions luminous ellipticals have flatter density distributions than low-luminosity ellipticals .

(iii) Finally, luminous ellipticals have lower mean density within $R_{\rm e}$ than low-luminosity ellipticals, a well known consequence of the Kormendy (1977) relation.

In this paper we presented the results of numerical N-body simulations of one- and two-component dissipationless collapses, focusing on their possible relevance to the origin of the weak homology and of the core/power-law dichotomy of ellipticals, i.e., we addressed points (i) and (ii) above, while it is quite obvious that point (iii) cannot be studied with dissipationless collapse simulations. Overall, our results suggest that dissipationless collapse is effective in producing weak structural homology, kinematic properties consistent with observations, and cores on scales remarkably similar to those observed. In particular:

• The end-products of one-component dissipationless collapses typically have projected surface brightness profile close to the de Vaucouleurs model (see also vA82; Londrillo et al. 1991; Dantas et al. 2002; Trenti et al. 2004). When fitted with the Sersic law over the radial range $0.1 \lesssim R/R_{\rm e} \lesssim 10$, the resulting profiles are characterized by index $3.6 \lesssim m \lesssim 8$; $m \gtrsim 5$ final states are obtained only for rather concentrated initial conditions.

• The end-products of collapses inside a dark matter halo present significant structural non-homology. The best-fit Sersic indices of the stellar projected surface density profile span the range $1.9 \lesssim m \lesssim 12$. Remarkably, the parameter m correlates with the amount of dark matter present within $R_{\rm e}$, being smaller for larger dark-to-visible mass ratios.

• The projected stellar density profiles are characterized by a break radius $0.01 \lesssim R_{\rm b}/R_{\rm e} \lesssim 0.1$ within which the profile is flatter than the inner extrapolation of the global best-fit Sersic law. Colder initial conditions lead to end-products with smaller $R_{\rm b}/R_{\rm e}$; in general, the resulting 'cores' are better detectable in high-m systems.

The results above indicate that dissipationless collapse is able to produce systems with projected density profiles remarkably similar to the observed surface brightness profiles, with high quality one-parameter Sersic fits even for low m values when non-negligible amounts of dark matter are present. In particular, in Fig. 10 we plot the (integrated) dark-to-total mass ratio $M_{\rm h}(r)/M_{\rm tot}(r)$ for the two-component simulations end-products. A clear dichotomy is apparent: while in low-m systems (dotted lines) the mass-to-light ratio increases significantly inwards, the opposite is true for systems with $m \gtrsim 3$ (with few exceptions). We also note that, while for $m \gtrsim 3$ systems the dark matter mass inside the half mass radius is of the same order as the visible mass, in accordance with observations (e.g. Bertin et al. 1994; Gerhard et al. 2001; Magorrian & Ballantyne 2001; Romanowsky et al. 2003; Treu & Koopmans 2004; Cappellari et al. 2006; Dekel et al. 2005; Samurović & Danziger 2005), for very low-m systems the dark matter is dominant.

According to the standard interpretation, the central cores observed in several bright ellipticals are a consequence of formation through merging, being produced by the interaction of binary supermassive black holes with a stellar cusp (Makino & Ebisuzaki 1996; Faber et al. 1997; Milosavljevic & Merritt 2001). Our results, in agreement with previous numerical explorations (vA82; May & van Albada 1984), indicate that a break in the profile at small radii and a flat central core are features produced naturally by dissipationless collapse. In particular, the fact that the size of the core is correlated (and the maximum central density anti-correlated) with the initial virial ratio is a direct consequence of Liouville Theorem[4] (e.g., May & van Albada 1984). The higher resolution of our simulations allowed us to investigate this effect in regions (down to $R \sim 0.01 R_{\rm e}$) comparable to those explored by high-resolution photometry of real ellipticals. In particular, the profiles of the end-products of our single-component simulations are remarkably similar to those of observed 'core' ellipticals. For instance, it is suggestive to compare the profile plotted in Fig. 4 (bottom, left panel) with that of the core-elliptical NGC 3348 (see fig. 10 of Graham et al. 2003), for which Trujillo et al. (2004) report best-fit $m \simeq 3.8$ and $R_{\rm b}/R_{\rm e} \simeq 0.016$. The fact that the end-products of our simulations reproduce very nicely the observed cores makes dissipationless collapse a plausible alternative to the binary black hole scenario for the origin of the cores. The next step of the present study would be the exploration with a hydro N-body code of the first stages of galaxy formation dominated by gaseous dissipation and the following feedback effects due to star formation.

[4] Hozumi, Burkert & Fujiwara (2000) pointed out that another consequence of the conservation of the phase-space density is that the initial anisotropy in the velocity distribution affects the final density profile at small radii. As shown by their spherically-symmetric dissipationless collapse simulations, smaller central cores are produced by more radially anisotropic collapses.

ACKNOWLEDGMENTS

We thank the anonymous Referee for useful comments. L.C and P.L. were supported by the MIUR grant CoFin 2004. C.N. and P.L. are grateful to CINECA (Bologna) for assistance with the use of the IBM Linux Cluster.

REFERENCES

Bender R., Burstein D., Faber S. M., 1993, ApJ, 411, 153
Bertin G., Ciotti L., Del Principe M., 2002, A&A, 386, 1491
Bertin G., et al. 1994, A&A, 292, 381
Binney J., 1982, MNRAS, 200, 951
Burstein D., Davies R.L., Dressler A., Faber S.M., Lynden-Bell D., 1988. In: *Towards understanding galaxies at large redshift; Proceedings of the Fifth Workshop of the Advanced School of Astronomy*, Dordrecht, Kluwer Academic Publishers.
Cappellari M., et al., 2006, MNRAS, 366, 1126
Ciotti L., 1991, A&A, 249, 99
Ciotti L., 1996, ApJ, 471, 68
Ciotti L., 1999, ApJ, 520, 574
Ciotti L., Bertin G., 1999, A&A, 352, 447
Ciotti L., Pellegrini S., 1992, MNRAS, 255, 561
Ciotti L., van Albada, T.S., 2001, ApJ, 552, L13
Caon N., Capaccioli M., D'Onofrio M., 1993, 265, 1013
Dantas C.C., Capelato H.V., de Carvalho R.R., Ribeiro A.L.B., 2002, A&A, 384, 772
Dehnen W., 1993, MNRAS, 265, 250
Dehnen W., 2000, ApJ, 536, L39
Dehnen W., 2002, Journal of Computational Physics, 179, 27
Dekel A., Stoehr F., Mamon G.A., Cox T.J., Novak G.S., Primack J.R., 2005, Nature, 437, 707
de Vaucouleurs G., 1948, Ann. d'Astroph., 11, 247
Eggen O.J., Lynden-Bell D., Sandage A.R., 1962, ApJ, 136, 748
Faber S.M., Jackson R.E., 1976, ApJ, 204, 668
Faber S.M., et al., 1997, AJ, 114, 1771
Ferrarese L., Merritt D., 2000, ApJ, 539, L9
Ferrarese L., van den Bosch F.C., Ford H.C., Jaffe W., O'Connell R.W., 1994, AJ, 108, 1598
Ferrarese L., et al., 2006, ApJS, in press (astro-ph/0602297)
Gebhardt K. et al., 2000, ApJ, 539, L13
Gerhard O., Kronawitter A., Saglia R.P., Bender R., 2001, AJ, 121, 1936
Graham A.W., Guzmán R., 2003, AJ, 125, 2936
Graham A.W., Erwin P., Trujillo I., Asensio Ramos A., 2003, ApJ, 125, 2951
Hernquist L., 1990, ApJ, 356, 359
Hozumi S., Burkert A., Fujiwara T., 2000, MNRAS, 311, 377
Kormendy J., 1977, ApJ, 218, 333
Lake G., 1983, ApJ, 264, 408
Lauer T.R., et al., 1995, AJ, 110, 2622
Londrillo P., Messina A., Stiavelli M., 1991, MNRAS, 250, 54

Londrillo P., Nipoti C., Ciotti L., 2003, In "Computational astrophysics in Italy: methods and tools", Roberto Capuzzo-Dolcetta ed., Mem. S.A.It. Supplement, vol. 1, p. 18
Magorrian J., Ballantyne, D., 2001, MNRAS, 322, 702
May A., van Albada, T.S., 1984, MNRAS, 209, 15
Makino J., Ebisuzaki T., 1996, ApJ, 465, 527
McGlynn T.A., 1984, ApJ, 281, 13
Merritt D., Navarro J.F., Ludlow A., Jenkins A., 2005, ApJ, 624, L85
Milosavljevic M., Merritt D., 2001, ApJ, 563, 34
Naab T., Johansson P.H., Efstathiou G., Ostriker J.P., 2005, submitted to ApJ (astro-ph/0512235)
Navarro J.F., Frenk C.S., White S.D.M., 1996, ApJ, 462, 563 (NFW)
Nipoti C., Londrillo P., Ciotti L., 2002, MNRAS, 332, 901
Nipoti C., Londrillo P., Ciotti L., 2003a, MNRAS, 342, 501 (NLC03)
Nipoti C., Stiavelli M., Treu T., Ciotti L., Rosati P., 2003b, MNRAS, 344, 748
Nipoti C., Treu T., Ciotti L., Stiavelli M., 2004, MNRAS, 355, 1119
Pellegrini S., 1999, A&A, 351, 487
Pellegrini S., 2005, MNRAS, 364, 169
Power C., Navarro J.F., Jenkins A., Frenk C.S., White S.D.M., Springel V., Stadel J., Quinn T., 2003, MNRAS, 338, 14
Plummer H.C., 1911, MNRAS, 71, 460
Prugniel P., Simien F., 1997, A&A, 321, 111
Robertson B., Cox T.J., Hernquist L., Franx M., Hopkins P.F., Martini P., Springel V., 2006, ApJ, 641, 21
Romanowsky A.J., Douglas N.G., Arnaboldi M., Kuijken K., Merrifield M.R., Napolitano N.R., Capaccioli M., Freeman K.C., 2003, Science, 301, 1696
Samurović S., Danziger I.J., 2005, MNRAS, 363, 769
Sersic J.L., 1968, Atlas de galaxias australes. Observatorio Astronomico, Cordoba
Tremaine S., Richstone D.O., Yong-Ik B., Dressler A., Faber S.M., Grillmair C., Kormendy J., Laurer T.R., 1994, AJ, 107, 634
Trenti M., Bertin G., van Albada T.S., 2005, A&A, 433, 57
Treu T., Koopmans L.V., 2004, ApJ, 611, 739
Trujillo I., Erwin P., Asensio Ramos A., Graham A.W., 2004, AJ, 127, 1917
Udry S., 1993, A&A, 268, 35
van Albada T.S., 1982, MNRAS, 201, 939 (vA82)
White S.D.M., Frenk C.S., 1991, ApJ, 379, 52
White S.D.M., Rees M.J., 1978, MNRAS, 183, 341